PROCEEDINGS of the
23rd International Congress on Acoustics
9 to 13 September 2019 in Aachen, Germany

Finite element analysis on the surface characteristics of acoustic resonators with thermal and viscous boundary layers

Naohisa INOUE*, Tetsuya SAKUMA

Graduate School of Frontier Sciences, The University of Tokyo, Japan

Abstract

The thermal and viscous boundary layers (TVBL) around a resonator's neck play important roles in the absorption, particularly when there is no porous material near the neck. This paper presents a simple implementation of a TVBL boundary condition for the three-dimensional finite element analysis of Helmholtz equation. The implementation is verified by comparing normal incidence absorption coefficients calculated and measured for slit-type resonators. Good agreement can be observed under the appropriate calculation setting. Subsequently, a detailed investigation is conducted on surface impedances of Helmholtz resonators composed of circular holes and square baffles. Numerical values are compared with analytical values based on the classical models such as Maa, Allard–Ingard and so on. It is demonstrated that the presented method convincingly captures the surface impedance on an acoustic resonator unless the TVBL thicknesses are much larger than the perforation diameter.

Keywords: Viscous and thermal boundary layer, Finite element method, Helmholtz resonator

1 INTRODUCTION

Predicting the absorption performance of resonators is of great interest for noise control engineers. The thermal and viscous boundary layers (TVBL) around a resonator's neck play important roles in the absorption, particularly when there is no porous material near the neck. Several papers have been dedicated to the numerical prediction of resonator's absorption performance. The recently proposed approaches have been based on computational fluid dynamics [1] or the viscothermal acoustic elements [2]. Accordingly, relatively high computation and implementation costs are required. This paper concerns another simple approach that is based on the equivalent boundary condition of TVBL in the conventional Helmholtz equation [3, 4]. Despite its effectiveness, the details of the implementation have not been presented, especially where giving the TVBL boundary condition. Furthermore, to the authors' best knowledge, three-dimensional analysis has not been performed yet. This may be caused by the apparent difficulty of evaluating the tangential Lhaplacian term for the viscous effect on the boundary.

This paper presents the finite element implementation of the TVBL boundary condition for three-dimensional frequency-domain problems. This implementation is applied to analyze the absorption characteristics of slit-type and Helmholtz resonators, and the appropriate calculation setting is clarified.

2 FINITE ELEMENT IMPLEMENTATION

2.1 TVBL Boundary Condition

The time convention is $e^{j\omega t}$ throughout this paper. The boundary condition taking the effect of thermal and viscous boundary layers into account is given in [5] as

$$\frac{\partial p}{\partial n} = -j\omega\rho_0 \left[\frac{1}{Z_\mathrm{n}} + (1+j) \left(\frac{R_\mathrm{t}}{\rho_0^2 c_0^2} - \frac{R_\mathrm{v}}{\rho_0^2 \omega^2} \nabla_\mathrm{tan}^2 \right) \right] p \tag{1}$$

where p, ρ_0, c_0, and Z_n are the sound pressure, air density, sound speed, and normal-incidence surface impedance, respectively. ∇_tan^2 is the Laplacian operator in the tangential plane of the boundary and $\partial/\partial n$ is the normal

*inoue@env-acoust.k.u-tokyo.ac.jp

derivative to the plane. R_t and R_v are the thermal and viscous resistances, which are related to the thicknesses of the thermal and viscous boundary layers, δ' and δ, as follows:

$$R_\mathrm{t} = \frac{1}{2}\rho_0\omega(\gamma-1)\delta', \quad \delta' = \sqrt{\frac{2\mu}{\rho_0\omega N_\mathrm{pr}}} \quad \text{and} \quad R_\mathrm{v} = \frac{1}{2}\rho_0\omega\delta, \quad \delta = \sqrt{\frac{2\mu}{\rho_0\omega}}, \tag{2}$$

where γ, μ, and N_pr are the heat capacity ratio, viscous coefficient, and Prandtl number of the air, respectively. Note that several signs in the above are modified from those in [5] owing to the time convention $e^{j\omega t}$. To simplify Eq. (1), it is rewritten as

$$\frac{\partial p}{\partial n} = -jk\beta p - (j\omega)^{3/2}c_\mathrm{T}p - (j\omega)^{-1/2}c_\mathrm{V}\nabla^2_\mathrm{tan}p \tag{3}$$

where β is the normalized admittance and the frequency-independent coefficients, c_T and c_V, are defined as

$$c_\mathrm{T} = \frac{\gamma-1}{c_0^2}\sqrt{\frac{\mu}{\rho_0 N_\mathrm{pr}}} \quad \text{and} \quad c_\mathrm{V} = \sqrt{\frac{\mu}{\rho_0}}. \tag{4}$$

Obviously, the TVBL boundary condition involves a fractional derivative in the time domain expression, which makes it difficult to use in time domain analysis. On the other hand, this paper focuses on the treatment of the boundary condition in frequency domain analysis.

2.2 Weak Formulation of the Helmholtz Equation

The weak form of the Helmholtz equation, $\nabla^2 p + k^2 p = 0$, is given as

$$\int_\Omega \nabla\delta p \cdot \nabla p dV - k^2 \int_\Omega \delta p \cdot p dV - \int_\Gamma \delta p \frac{\partial p}{\partial n} dS = 0, \tag{5}$$

where δp is the admissible variation and ∇ is the nabla operator. Substituting Eq. (2) into Eq. (3), the following equation is obtained:

$$\int_\Omega \nabla\delta p \cdot \nabla p dV - k^2 \int_\Omega \delta p \cdot p dV + jk\beta \int_\Gamma \delta p \cdot p dS + (j\omega)^{3/2} c_\mathrm{T} \int_\Gamma \delta p \cdot p dS + (j\omega)^{-1/2} \int_\Gamma \delta p \cdot \nabla^2_\mathrm{tan} p dS = 0. \tag{6}$$

The main difficulty of the implementation is to evaluate the fifth boundary integral term. Although the interpolation function must be differentiable twice or more to evaluate the term directly, this requirement can be reduced by applying Green's first identity in two-dimensions as follows:

$$\int_\Gamma \delta p \cdot \nabla^2_\mathrm{tan} p dS = -\int_\Gamma \nabla_\mathrm{tan}\delta p \cdot \nabla_\mathrm{tan} p dS + \int_{\partial\Gamma} \delta p \cdot (\nabla_\mathrm{tan} p \cdot \underline{n}_\mathrm{c}) dC \tag{7}$$

where ∇_tan is the gradient operator in the tangential plane and $\underline{n}_\mathrm{c}$ is the outward normal vector to the contour of the boundary surface. Accordingly, the energy dissipation along the contour should be evaluated in the latter term, which makes the global system matrix asymmetric.

2.3 Evaluation of the Tangential Gradient Term

This section presents an algorithm to evaluate the tangential gradient term in the generalized curvilinear local coordinate set in the boundary elements. In the first, let us consider the local coordinate (ξ, η) that is usually set for the numerical integration in the finite element method. Then the global coordinate values in an element are interpolated with the shape functions $N_i(\xi,\eta)$ and the nodal coordinate values (x_i, y_i, z_i) as $x = \sum_i N_i(\xi,\eta)x_i$ and so on. The covariant basis vectors of the tangential plane, $\underline{e}_\xi$ and $\underline{e}_\eta$, are given as follows.

$$\underline{e}_\xi(\xi,\eta) = \frac{\partial x(\xi,\eta)}{\partial\xi}\underline{e}_x + \frac{\partial y(\xi,\eta)}{\partial\xi}\underline{e}_y + \frac{\partial z(\xi,\eta)}{\partial\xi}\underline{e}_z, \quad \underline{e}_\eta(\xi,\eta) = \frac{\partial x(\xi,\eta)}{\partial\eta}\underline{e}_x + \frac{\partial y(\xi,\eta)}{\partial\eta}\underline{e}_y + \frac{\partial z(\xi,\eta)}{\partial\eta}\underline{e}_z \tag{8}$$

where $\underline{e}_x, \underline{e}_y, \underline{e}_z$ are the unit basis vector of the global Cartesian coordinate. On the other hand, the contravariant basis vectors of the tangential plane, $\underline{e}^\xi$ and $\underline{e}^\eta$, are given as follows:

$$\underline{e}^\xi = \frac{\underline{e}_\eta \times \underline{e}_\zeta}{\underline{e}_\xi \cdot (\underline{e}_\eta \times \underline{e}_\zeta)}, \quad \underline{e}^\eta = \frac{\underline{e}_\zeta \times \underline{e}_\xi}{\underline{e}_\eta \cdot (\underline{e}_\zeta \times \underline{e}_\xi)}. \tag{9}$$

where $\underline{e}_\zeta$ is the normal vector to the tangential plane defined as $\underline{e}_\zeta = \underline{e}_\xi \times \underline{e}_\eta$. The tangential gradient vectors in Eq.(4) can be expressed by using the terms of the general curvilinear local coordinate as follows.

$$\nabla_{\tan}\delta p = \frac{\partial \delta p}{\partial \xi}\underline{e}^\xi + \frac{\partial \delta p}{\partial \eta}\underline{e}^\eta, \quad \nabla_{\tan} p = \frac{\partial p}{\partial \xi}\underline{e}^\xi + \frac{\partial p}{\partial \eta}\underline{e}^\eta \tag{10}$$

Finally, the first term of Eq.(4) can be rewritten as

$$\int_\Gamma \nabla_{\tan}\delta p \cdot \nabla_{\tan} p dS = \int_\eta \int_\xi \left[\frac{\partial \delta p}{\partial \xi}\frac{\partial p}{\partial \xi}\underline{e}^\xi \cdot \underline{e}^\xi + \left(\frac{\partial \delta p}{\partial \xi}\frac{\partial p}{\partial \eta} + \frac{\partial \delta p}{\partial \eta}\frac{\partial p}{\partial \xi} \right) \underline{e}^\xi \cdot \underline{e}^\eta + \frac{\partial \delta p}{\partial \eta}\frac{\partial p}{\partial \eta}\underline{e}^\eta \cdot \underline{e}^\eta \right] |J| d\xi d\eta \tag{11}$$

where $|J|$ is the Jacobian at each point in an element and defined as $|J| = |\underline{e}_\xi \times \underline{e}_\eta|$. The integrand in Eq.(11) can be easily evaluated at the gauss quadrature points. Furthermore, the second term of Eq.(4) can be rewritten as

$$\int_{\partial\Gamma} \delta p \cdot (\nabla_{\tan} p \cdot \underline{n}_c) dS = \int_{\xi(,\eta)} \delta p \left(\frac{\partial p}{\partial \xi}\underline{e}^\xi \cdot \underline{n}_c + \frac{\partial p}{\partial \eta}\underline{e}^\eta \cdot \underline{n}_c \right) |J| d\xi(,d\eta). \tag{12}$$

This contour integral should be calculated for surface elements adjacent to $\partial\Gamma$.

3 PREDICTION OF THE NORMAL-INCIDENCE ABSORPTION COEFFICIENT

3.1 Slit-type Resonators

In [3], the TVBL boundary condition was implemented in the two-dimensional boundary element method (BEM), where the term of $\nabla^2_{\tan} p$ was directly evaluated using the finite differences of sound pressures between neighboring elements. This implementation was applied to estimate the normal-incidence absorption coefficients of slit-type resonators, and the results were confirmed to be in good agreement with measured values. In this section, to clarify the appropriate setting of the implementation, slit-type resonators are examined by the three-dimensional finite element method (FEM), and the results are compared with BEM results and the measured values in [3].

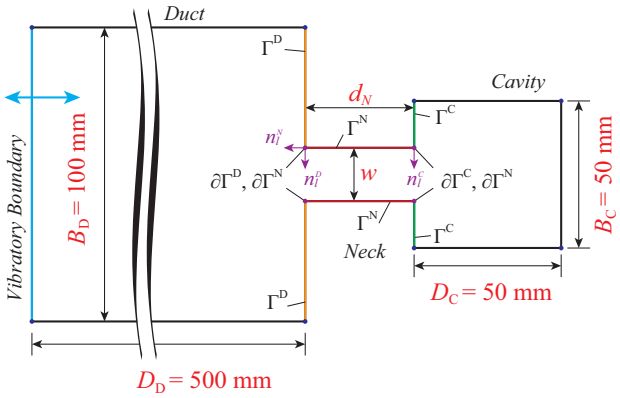

Figure 1. Horizontal geometry of the duct with a slit-type resonator.

In the FEM analysis, a 100-mm-square duct with a slit-type resonator is modeled, where all surfaces are as-sumed to be rigid ($\beta = 0$). Figure 1 shows the horizontal geometry of the model and the notation of the boundaries. These conditions correspond to those of the measurement in [3]. As a broad setting, the TVBL boundary condition is given to the end surface of the duct (Γ_D), the front surface of the cavity (Γ_C), and the side, upper, and bottom surfaces of the slit neck (Γ_N). On the contours of Γ_D and Γ_C, $\nabla_{\tan} p \cdot \underline{n}_c$ is zero except along the edges of the neck. Thus, contour integrals are evaluated along the edges ($\partial\Gamma_D, \partial\Gamma_C, and \partial\Gamma_N$). Second-order prism and hexahedral elements are used, and a fine mesh is applied as illustrated later in Fig. 4(a). The normal-incidence absorption coefficients are calculated by the transfer function method at 1/24-octave band center frequencies [6].

Figure 2 shows the calculated and measured results for four slit-type resonators with different combinations of the width and depth of the neck. The FEM results are given for three different settings, and the BEM and measured results are cited from [3]. The FEM results with the above broad TVBL setting are represented by red lines. The calculated values for the 4-mm-width slit correspond relatively well with the BEM and measured ones, whereas those for the 2-mm-width slit are slightly larger than the others. Nevertheless, this TVBL setting for the FEM seems reasonably reliable.

Next, a narrow TVBL setting only in the neck (Γ_N) is examined. As can be seen from the results represented by blue lines, the calculated values are considerably greater than those with the broad setting. This overestimation of the absorption coefficient may be caused by intensification of the edge potential around the openings of the neck due to the lack of a tangential drag force on Γ_D and Γ_C.

Therefore, it is suggested that the TVBL boundary condition should be given to two surfaces along an edge. If the asymmetric contour integral term for edges, Ic, can be neglected, the calculation becomes more efficient. However, the absorption coefficients calculated without Ic, represented with green lines, are lower than the red lines. This demonstrates that the energy dissipation at edges around a resonator's neck must be considered to predict the absorption coefficient accurately.

In the above calculation, fine meshes were used because the acoustic field around the neck is expected to change sharply. Figure 3 shows the results calculated with the fine and coarse meshes illustrated in Fig. 4. As a fixed condition, two hexahedral elements are generated in the direction of the slit width. The maximum lengths around the neck are 2 and 10 mm for fine and coarse meshes, respectively. It can be seen that the

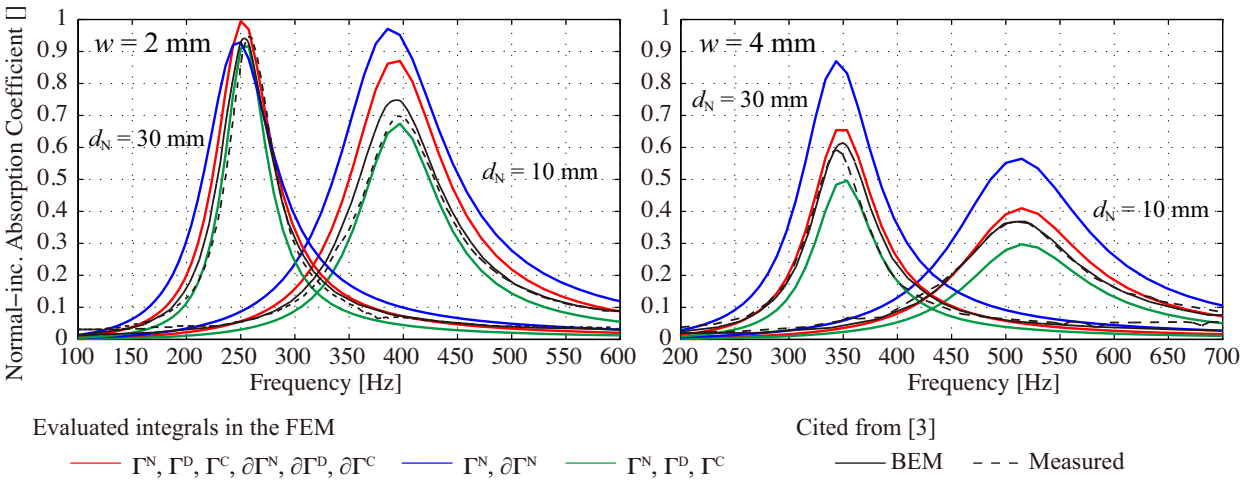

Figure 2. Normal-incidence absorption coefficients of four slit-type resonators calculated by the FEM with three different settings. The BEM and measured values for PVC are cited from [3].

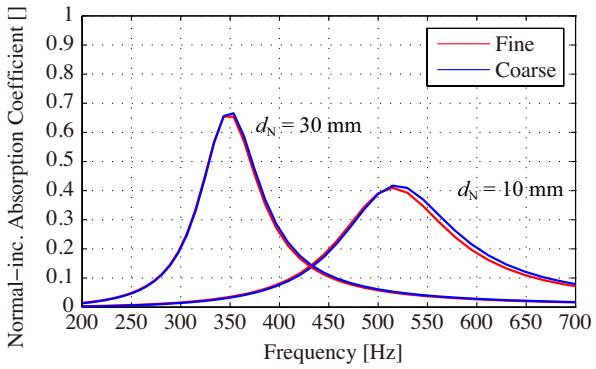

Figure 3. Normal-incidence absorption coefficient calculated with two different mesh resolutions.

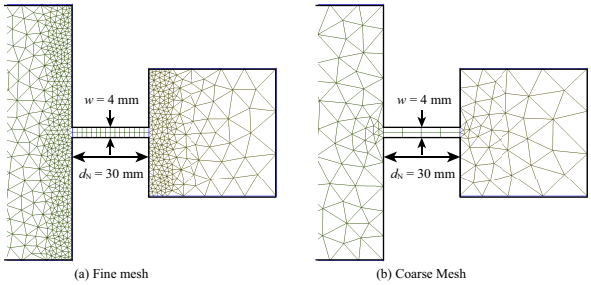

Figure 4. Meshes for the examination of effects of mesh resolution around neck.

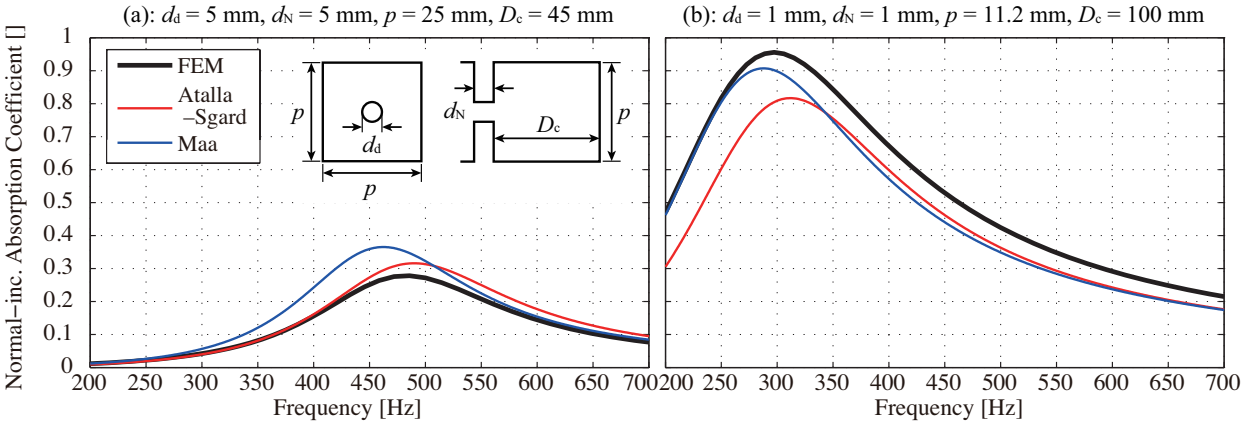

Figure 5. Normal-incidence absorption coefficients calculated for two Helmholtz resonators with different sizes, Types (a) and (b).

results for the coarse mesh are slightly greater than those for the fine mesh, but the difference is not significant when predicting the absorption coefficient.

3.2 Helmholtz Resonators

As a typical example of three-dimensional resonators, Helmholtz resonators are analyzed under a similar setting to that in the previous section, where the cross sections of the cavity and duct are identical and square. In the FEM calculation, the TVBL boundary condition is given to the front and back surfaces of the perforated baffle and the cylindrical surface of the neck. The normalized admittance β is assumed to be zero for all surfaces. The FEM results are compared with the existing theoretical models of Atalla and Sgard [7] and Maa [8]. The resistance and inertial correction terms are approximately derived for periodic resonators in the Atalla—Sgard model and for a single resonator in the Maa model. Note that the resistance correction of the Maa model is based on [7].

Figure 5 shows the calculated results for two resonators with different sizes. It can be seen that all the theoretical and FEM results are relatively correlated but slightly different in terms of the peak value and frequency. The sound field in the duct is equivalent to the normal-incidence field over the periodic resonators. However, the

FEM results are closer to the Atalla--Sgard model for Type (a) but closer to the Maa model for Type (b). This inconsistency implies that the interactive motion of the neck and cavity considerably affects the resistance and inertance corrections for the neck's impedance. From this viewpoint, the FEM may be advantageous because the effects of the interaction are automatically incorporated.

4 PREDICTION OF THE SURFACE IMPEDANCES

This section discusses the surface impedance of Helmholtz resonators in more detail in order to clarify the applicable condition of the TVBL boundary condition. In this study, Maa model is employed as the theoretical reference. The analytical effective density for the cylindrical pore, ρ', shows the low- and high-frequency asymptotic behaviors as follows.

$$\rho' = \rho_0 \left[1 - \frac{2}{s\sqrt{-j}} \frac{J_1(s\sqrt{-j})}{J_0(s\sqrt{-j})} \right]^{-1} \simeq \begin{cases} \dfrac{4}{3}\rho_0 + \dfrac{1}{j\omega}\dfrac{8\eta}{r^2}, & \text{for } \omega < \dfrac{18\eta}{\rho_0 r^2} = \omega_{\mathrm{L}} \quad (13) \\ \rho_0 + \dfrac{1}{r}\sqrt{\dfrac{2\rho_0\eta}{\omega}}(1-j), & \text{for } \omega > \dfrac{32\eta}{\rho_0 r^2} = \omega_{\mathrm{H}} \quad (14) \end{cases}$$

4.1 Numerical Models of Helmholtz Resonators

Figure 6 shows the numerical models for calculating the surface impedance by transfer function method. The cross-section of the tube is the square with D mm side. The perforation is placed in the center of the square. In order to better understanging, two neck models of Helmholtz resonators are employed: in model A, ρ' is given as the air density inside the resonator neck, whereas in model B, ρ_0 is given and the TVBL boundary condition is given to the peripheral surface of the neck. The TVBL boundary condition is give to the baffle surfaces in both models. For the sake of completeness, the sound pressures averaged over the cross-section are used for the transfer function method to exclude any scattered oblique waves.

The calculation was excuted at 1/3 octave band center frequencies with the following parameters. Hole radius is set to 0.25, 0.5, 1.0 and 2.0 mm. Two combinations of neck length, L mm, and hole pitch, D mm, are set: (a)$(L,D) = (1,10)$ and (b)$(L,D) = (4,20)$.

4.2 Results and Discussions

Figure 7 shows the surface resistance, reactance and the absorption coefficient under the normal incidence condition. As a general tendency of the resistance, model A below ω_{L} and model B above ω_{H} show good

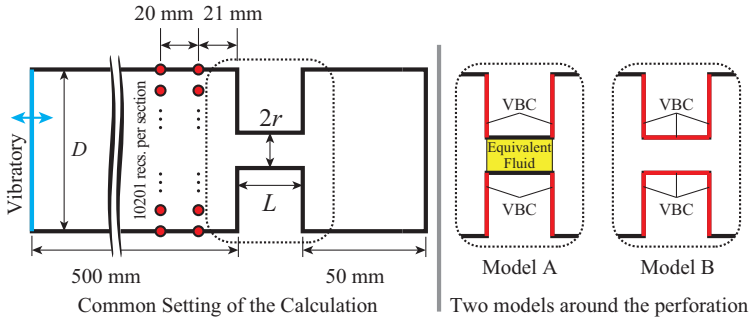

Figure 6. Calculation settings of the surface impedances. VBC stands for viscous boundary layer boundary condition.

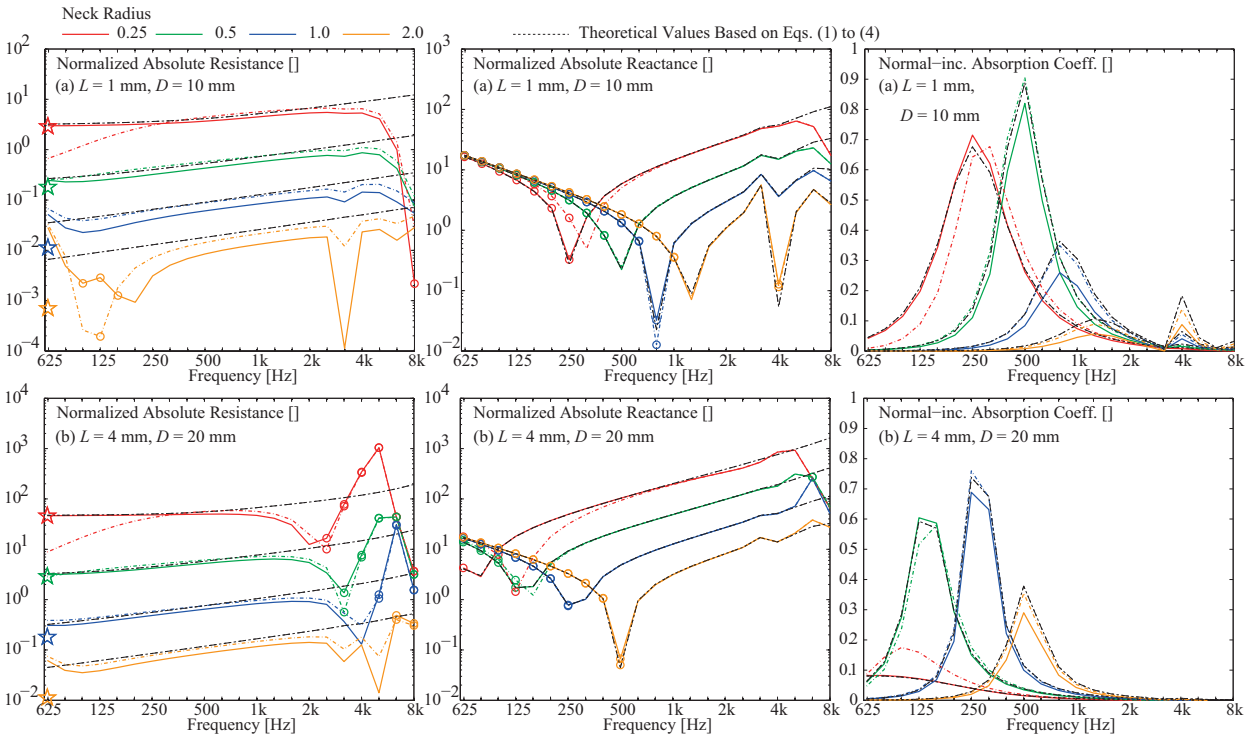

Figure 7. Normalized absolute surface resistance and reactance and normal-incidence absorption coefficient calculated for different combinations of neck length(L), neck radius(r) and hole pitch(D). Circle markers denote that the value was negative. Star markers denote the lower limit of surface resistance ($8\eta LD^2/\pi r^4$). Solid and chain lines are for model A and B, respectively.

correlation with the theoretical reference. The resistance of model A becomes lower than the theoretical reference in entire frequency range above ω_L. On the other hand, model B does not capture the low-frequency asymptotic behavior. Regarding the reactance, in particular for r = 0.25 mm, the model B does not reflect the apparent increase of the mass-reactance indicated as the factor 4/3 of Eq.(13), which causes the shift of the absorption peak. These tendencies demonstrate that the reliability of the TVBL boundary condition becomes lower below ω_L for the cylindrical pores. Besides, the resistances determined by the numerical calculations become negative in the high frequencies in several cases. A cause of this unpreferable behavior may be due to the approximation in the derivation of the TVBL boundary condition. This point should be investigated more carefully in future work.

5 CONCLUSION

This paper presented and verified the finite element modeling of acoustic resonators with thermal and viscous boundary layers. It was confirmed that the TVBL boundary condition should be given not only to the side surfaces in the resonator's neck but also to the front and back surfaces of the perforated baffles. Furthermore, the energy dissipation at the neck's edges was not negligible. Thus, an asymmetric matrix equation should be solved. Numerical methods are advantageous for predicting the absorption performance of resonators not only because of their capability of handling resonators with complex shapes, but also because the resistance and reactance corrections are automatically incorporated, reflecting the acoustic field around the neck. However, it should be emphasized that the TVBL boundary condition should be applied with great care for

some frequency ranges. In the low frequencies, the TVBL boundary condition cannot express the low-frequency asymptotic behavior of the effective density in the pores. On the other hand, in the high frequencies, the TVBL boundary condition employed in this paper may involve some erroneous approximation in its derivation, which cause physically unreasonable behavior in the surface resistance. In future work, the presented results should be verified by comparison with those of more exact methods such as those in [1, 2].

REFERENCES

[1] J. S. Bolton and N. Kim, "Use of CFD to calculate the dynamic resistive end and correction for microperforated materials," Acoust. Aust., 38, 134–139 (2010).

[2] W. R. Kampinga, Y. H. Wijnant and A. de Boer, "An efficient finite element model for viscothermal acoustics," Acta Acustica united with Acustica, 97, 618–631 (2011).

[3] K. Monjyugawa, M. Terao and H. Sekine, "Numerical analyses and high precision experiments on acoustic resistances of slit resonators," Proc. Spring Meet. Acoust. Soc. Jpn., 639–640 (2000) (in Japanese).

[4] S. Sakamoto, H. Mukai and H. Tachibana, "Numerical study on sound absorption characteristics of resonance-type brick/block walls," J. Acoust. Soc. Jpn., 21, 9–15 (2000).

[5] P. M. Morse and K. U. Ingard, Theoretical Acoustics, (Princeton University Press, New Jersey, 1968), Chap. 6.

[6] N. Inoue and T. Sakuma, "Numerical investigation of effect of support conditions of poroelastic materials in impedance tube measurement," Acoust. Sci. & Tech., 38, 213–221 (2017).

[7] N. Atalla and F. Sgard, "Modeling of perforated plates and screens using rigid frame porous models," J. Sound Vib., 303, 195–208 (2007).

[8] D. Maa, "Potential of microperforated panel absorber," J. Acoust. Soc. Am., 104, 2861–2866 (1998).